

# Legendre spectral element method with nearly incompressible materials

Y. V. Peet<sup>a,b,\*</sup>, P. F. Fischer<sup>b</sup>

<sup>a</sup>*Department of Engineering Sciences and Applied Mathematics, Northwestern University, Evanston, IL 60208-3125, USA*

<sup>b</sup>*Mathematics and Computer Science Division, Argonne National Laboratory, Argonne, IL 60439, USA*

---

## Abstract

We investigate convergence behavior of a spectral element method based on Legendre polynomial-based shape functions solving three-dimensional linear elastodynamics equations for a range of Poisson's ratios of a material. We document uniform convergence rates independent of Poisson's ratio for a wide class of problems with both straight and curved elements, demonstrating the locking-free properties of the spectral element method with nearly incompressible materials. Also documented is the second-order temporal convergence of the Newmark integration scheme for time-dependent formulation for a range of Poisson's ratios.

*Keywords:* spectral element method; nearly incompressible materials; Poisson locking; Newmark time integration

---

---

\*Corresponding author: Tel.: +1 847 467 3451.

*Email addresses:* `y-peet@northwestern.edu` (Y. V. Peet), `fischer@mcs.anl.gov` (P. F. Fischer)

## 1. Introduction

Spectral element methods (SEM), which essentially represent a hybrid between finite-element methods (FEM) and spectral methods, have received increased attention during the past two decades because they retain an exponential accuracy of global spectral methods while allowing for a geometrical flexibility of  $h$ -type FEM. Originally introduced in the field of computational fluid dynamics [1, 2, 3], spectral element methods have been adopted for elastostatics [4, 5] and elastodynamics [6, 7, 8] problems, modeling of elastic wave propagation in seismology [9, 10, 11], medical diagnostics [12], and damage detection [13] by high-frequency ultrasound excitation.

Spectral element methods are similar to  $hp$  finite-element methods [14] in that grid refinement can be achieved both by increasing the number of elements ( $h$ -refinement) and by increasing the polynomial order of approximation within each element ( $p$ -refinement). The difference is in the choice of bases and quadrature rules for evaluating the integrals in the Galerkin formulation. It is well known that higher-order  $p$  and  $hp$  finite-element methods, besides having superior convergence properties, possess an additional advantage of eliminating locking present with low-order FEM [15, 16]. Locking is defined as significant deterioration or complete loss of convergence when a certain parameter approaches its limiting value [17, 18].

One important type of locking is volumetric, or Poisson, locking, which occurs when Poisson's ratio  $\nu$  of an isotropic elastic material approaches 0.5. As this situation occurs, the divergence of a displacement field approaches zero, representing the condition of material incompressibility. Nearly incompressible behavior is peculiar to viscoelastic materials such as rubberlike polymers

and elastomers (polyamide, polystyrene, polycarbonate, polyurethane, butadiene, natural rubber, etc.) [19]. In addition, soft biological tissues such as endothelium, smooth muscle cells, and adventitia forming the blood vessel walls exhibit similar rubberlike behavior [20] and are often modeled as elastic incompressible materials [21, 22, 23].

When nearly incompressible materials are modeled with low-order  $h$ -type finite elements, Poisson locking results in a poor numerical solution that does not improve, or improves very slowly, with grid refinement [18, 24]. Locking occurs because of the need to satisfy the divergence-free constraint on displacements, one per element, which, in the case of  $h$ -refinement with low  $p$ , results in a number of constraints comparable to the number of degrees of freedom [25, 26]. To remedy the situation, one must reduce the number of constraints per degree of freedom [27]. To do so, one invokes special numerical techniques of varying difficulty, such as reduced/selective integration [28], field-consistent approach [29], or mixed methods, where the divergence constraint is introduced through a Lagrange multiplier [30].

Higher-order  $p$  and  $hp$  methods naturally avoid the locking phenomenon without the need for ad hoc numerical techniques because of the elevated number of degrees of freedom per element and inherently low constraint ratio. Researchers have shown theoretically [17, 18, 31] and demonstrated numerically [18, 25, 32] that in the  $p$  and  $hp$  versions of FEM the error measured in the energy norm converges at the same rate independent of Poisson's ratio. Spectral element methods, because of their close relation to  $hp$ -FEM, would be expected to retain the locking-free properties associated with higher-order approximation. In spite of a popularity of spectral element methods, how-

ever, neither theoretical nor computational studies of their behavior with nearly incompressible materials in its original (displacement) formulation have been performed.

Pavarino et al. theoretically analyzed the condition number of a preconditioned matrix operator for Legendre spectral element discretization of displacement formulation for compressible materials [4] and mixed formulation for incompressible materials [5, 33, 34]. Sprague et al. documented computational studies of convergence of Legendre spectral element formulation for a 1D Timoshenko beam [35] and 2D Reissner-Mindlin plate [36] using Poisson's ratio  $\nu = 0.3$ . Dong and Yosibash [8] computationally investigated convergence of Jacobi spectral element formulation with 3D steady and unsteady elasticity equations, also using  $\nu = 0.3$ . Few other studies with spectral elements, mostly with application to seismology, considered Earth-like solids with Poisson's ratio of 0.25 to 0.33 [7, 9, 10, 11], without documenting the convergence and error behavior.

The main goal of this paper is to investigate convergence properties of Legendre spectral element formulation computationally for steady and unsteady linear elasticity problems for a range of Poisson's ratios, from compressible ( $\nu = 0.3$ ) to nearly incompressible (up to  $\nu = 0.4999999999$ ). The novelty of the current paper, in addition to investigating locking behavior with respect to spectral elements as opposed to finite elements, consists in addressing the issue of locking for time-dependent problems, which has never been done before for neither spectral or finite-element methods.

The paper is organized as follows. In Section 2, we present the governing equations and their spatial and temporal discretization. In Section 3, we

look at numerical examples of steady elasticity problems with straight and curved elements. In Section 4, we consider an unsteady problem. In Section 5, we draw conclusions.

## 2. Problem Formulation

In this section, we present the problem formulation, including governing equations and their numerical discretization.

### 2.1. Equations and the variational form

We consider time-dependent linear elasticity equations

$$\rho \frac{\partial^2 \mathbf{u}}{\partial t^2} + c \frac{\partial \mathbf{u}}{\partial t} = \nabla \cdot \sigma + \mathbf{f}, \quad (1)$$

where  $\rho$  is the mass density,  $c$  is the viscous damping coefficient,  $\mathbf{u}$  is the displacement vector,  $t$  is the time,  $\sigma$  is the Cauchy stress tensor, and  $\mathbf{f}$  is the body force per unit volume. The method proceeds by casting Eq. (1) into an equivalent variational form. Let  $\Omega \in R^d$ ,  $d = 2, 3$ , be a domain of interest and  $\partial \Omega = \partial \Omega_D \cup \partial \Omega_N$  be its boundary decomposed into parts with Dirichlet and Neumann (traction) boundary conditions. Define the following proper subspaces of the  $H^1(\Omega)$  Sobolev space (space of functions square-integrable over  $\Omega$  whose first spatial derivatives are also square-integrable over  $\Omega$ ):

$$\begin{aligned} X &= \{\mathbf{v}(\mathbf{x}, t) \in H^1(\Omega)^d : \mathbf{v}(\mathbf{x}, t)|_{\partial \Omega_D} = \mathbf{u}_D(\mathbf{x}, t)\}, \\ X_0 &= \{\mathbf{v}(\mathbf{x}, t) \in H^1(\Omega)^d : \mathbf{v}(\mathbf{x}, t)|_{\partial \Omega_D} = 0\}. \end{aligned} \quad (2)$$

Then the variational formulation of the linear elasticity problem is as follows:

Find the displacement field  $\mathbf{u}(\mathbf{x}, t) \in \mathbf{X}$  such that  $\forall \mathbf{v}(\mathbf{x}, t) \in \mathbf{X}_0$

$$\begin{aligned} \int_{\Omega} \rho \frac{\partial^2 \mathbf{u}}{\partial t^2} \cdot \mathbf{v} d\Omega &+ \int_{\Omega} c \frac{\partial \mathbf{u}}{\partial t} \cdot \mathbf{v} d\Omega = \\ - \int_{\Omega} \sigma(\mathbf{u}) : \epsilon(\mathbf{v}) d\Omega &+ \int_{\partial \Omega_N} \mathbf{t} \cdot \mathbf{v} d\Gamma + \int_{\Omega} \mathbf{f} \cdot \mathbf{v} d\Omega. \end{aligned} \quad (3)$$

Here  $\mathbf{t}$  is the external traction force applied on  $\partial\Omega_N$ , and  $\epsilon(\mathbf{v}) = \frac{1}{2}[\nabla\mathbf{v} + (\nabla\mathbf{v})^T]$  is the linearized strain tensor. The vector and tensor inner products are defined as

$$\mathbf{u} \cdot \mathbf{v} = \sum_{i=1}^d u_i v_i, \quad (4)$$

$$\sigma(\mathbf{u}) : \epsilon(\mathbf{v}) = \sum_{i=1}^d \sum_{j=1}^d \sigma_{ij}(\mathbf{u}) \epsilon_{ij}(\mathbf{v}). \quad (5)$$

For linear elasticity, constitutive equations arise from Hooke's law,

$$\sigma = 2\mu\epsilon + \lambda \operatorname{tr}(\epsilon) \mathbf{I}, \quad (6)$$

where

$$\mu = \frac{E}{2(1+\nu)}, \quad (7)$$

$$\lambda = \frac{E\nu}{(1+\nu)(1-2\nu)} \quad (8)$$

for 3D isotropic materials and 2D plane strain formulation, and

$$\lambda = \frac{E\nu}{(1+\nu)(1-\nu)} \quad (9)$$

for 2D plane stress formulation,  $E$  is Young's modulus,  $\nu$  is Poisson's ratio,  $\operatorname{tr}()$  denotes the trace, and  $\mathbf{I}$  is the identity matrix. Introducing constitutive relations (6) into Eq. (5) leads to

$$\sigma(\mathbf{u}) : \epsilon(\mathbf{v}) = 2\mu(\epsilon(\mathbf{u}) : \epsilon(\mathbf{v})) + \lambda \operatorname{div}\mathbf{u} \operatorname{div}\mathbf{v}. \quad (10)$$

We denote

$$B_\nu(\mathbf{u}, \mathbf{v}) = \int_{\Omega} [2\mu(\epsilon(\mathbf{u}) : \epsilon(\mathbf{v})) + \lambda \operatorname{div}\mathbf{u} \operatorname{div}\mathbf{v}] d\Omega \quad (11)$$

as the bilinear form of linear elasticity.

## 2.2. Spatial discretization

In the spectral element method, the computational domain  $\Omega$  is decomposed into a set of nonoverlapping subdomains (elements)  $\Omega = \cup_{e=1}^{\mathcal{E}} \Omega^e$ . In the current method, we assume that for each  $\Omega^e$  there exists an affine transformation  $\hat{\Omega} = \phi^e(\Omega^e)$  into the reference element  $\hat{\Omega} = [-1, +1]^d$ , implying that  $\Omega^e$  are hexahedral. Other choices (prismatic, tetrahedral, etc.) are available [8, 37], but they will not be pursued here. On the reference element  $\hat{\Omega}$  we introduce  $Q_p(\hat{\Omega})$ , the space of polynomial functions of degree  $p$  in each spatial variable, and restrict the trial and test functions  $\mathbf{u}$  and  $\mathbf{v}$  in each element  $\Omega^e$  to the finite-dimensional spaces  $\mathbf{X}^p$  and  $\mathbf{X}_0^p$ ,

$$\begin{aligned} \mathbf{X}^p &= \{\mathbf{v}(\mathbf{x}, t) \in \mathbf{X} : v_i|_{\Omega^e} = \psi \circ \phi^e, \psi \in Q_p(\hat{\Omega}), i = 1, \dots, d\}, \\ \mathbf{X}_0^p &= \{\mathbf{v}(\mathbf{x}, t) \in \mathbf{X}_0 : v_i|_{\Omega^e} = \psi \circ \phi^e, \psi \in Q_p(\hat{\Omega}), i = 1, \dots, d\}, \end{aligned} \quad (12)$$

where  $f \circ g$  denotes a function composition. The basis functions for the polynomial space  $Q_p(\hat{\Omega})$  are chosen to be the tensor product of one-dimensional Lagrange interpolating polynomials  $h_i(r)$ ,  $r \in [-1, +1]$ , on the Gauss-Lobatto-Legendre (GLL) quadrature points  $\xi_m \in [-1, +1]$ ,  $i, m = 0, \dots, p$ , corresponding to a nodal basis. Let  $h_i(r)$  be the Lagrange interpolating polynomial satisfying  $h_i(\xi_m) = \delta_{im}$ . Every function in  $Q_p(\hat{\Omega})$  is represented as a tensor product

$$f(\mathbf{x}, t)|_{\hat{\Omega}} = \sum_{i=0}^p \sum_{j=0}^p \left\{ \sum_{k=0}^p \right\} f_{ij\{k\}}^e(t) h_i(r) h_j(r) \{ h_k(r) \}, \quad (13)$$

where  $f_{ij\{k\}}^e(t)$  are unknown expansion coefficients and curly brackets contain the extra terms that arise in three dimensions. Spatial derivatives of a function in  $Q_p(\hat{\Omega})$  can be defined analogously through the derivatives of the

corresponding Lagrange polynomials:

$$\frac{\partial f}{\partial x_1}(\mathbf{x}, t)|_{\hat{\Omega}} = \sum_{i=0}^p \sum_{j=0}^p \left\{ \sum_{k=0}^p \right\} f_{ij\{k\}}^e(t) h_i'(r) h_j(r) \{h_k(r)\}. \quad (14)$$

The current choice of basis functions allows for an efficient quadrature implementation. In addition, it is continuous across subdomain interfaces [38].

The quadrature rules are defined as

$$\int_{\hat{\Omega}} f g d\hat{\Omega} = \sum_{i=0}^p \sum_{j=0}^p \left\{ \sum_{k=0}^p \right\} f_{ij\{k\}}^e g_{ij\{k\}}^e \sigma_i \sigma_j \{\sigma_k\} \quad (15)$$

and

$$\int_{\Omega} f g d\Omega = \sum_{e=1}^{\mathcal{E}} \sum_{i,j,\{k\}=0}^p (f \circ \phi^e)_{ij\{k\}} (g \circ \phi^e)_{ij\{k\}} |J^e|_{ij\{k\}} \sigma_i \sigma_j \{\sigma_k\}, \quad (16)$$

where  $\sigma_i$  is the GLL quadrature weight associated with  $\xi_i$  and  $|J^e|_{ij\{k\}}$  is the Jacobian of the transformation  $\phi^e$  at the point  $(\xi_i, \xi_j, \{\xi_k\})$ . Thus, for a bilinear form  $\int_{\Omega} \mathbf{u} \cdot \mathbf{v} d\Omega$  we can write

$$\int_{\Omega} \mathbf{u} \cdot \mathbf{v} d\Omega = \underline{\mathbf{v}}^T \mathbf{B} \underline{\mathbf{u}}, \quad (17)$$

where  $\underline{\mathbf{u}}, \underline{\mathbf{v}}$  are the vectors with dimensions  $\mathcal{N} = d\mathcal{E}(p+1)^d$  of the corresponding expansion coefficients  $u_{ij\{k\}m}^e, v_{ij\{k\}m}^e, i, j, \{k\} = 0, \dots, p, m = 1, \dots, d, e = 1, \dots, \mathcal{E}$ , and  $\mathbf{B}$  is the (diagonal) mass matrix. Quadrature for the surface integral  $\int_{\partial\Omega_N} \mathbf{t} \cdot \mathbf{v} d\Gamma$  is defined similar to Eq. (16) using summation over the surface nodes on  $\partial\Omega_N$  with the corresponding quadrature weights and surface Jacobians in place of the volumetric ones. Using the definition of Eq. (14) for spatial derivatives, one can analogously define discrete quadrature for a bilinear form of linear elasticity  $B_{\nu}(\mathbf{u}, \mathbf{v})$  of Eq. (11), resulting in a symmetric, positive-definite stiffness matrix  $\mathbf{A}$ . Although the



stiffness matrix is no longer diagonal, the corresponding matrix-vector products can be efficiently evaluated in  $O(p^{d+1})$  operations if one retains the matrix tensor-product form in favor of its explicit formation [39]. Applying the corresponding numerical quadrature rules to every integral in the continuous Eq. (3), one can reformulate the original variational problem in discrete form: Find  $\underline{\mathbf{U}}(t) \in R_0^\mathcal{N}$  such that  $\forall \underline{\mathbf{v}}(t) \in R_0^\mathcal{N}$

$$\underline{\mathbf{v}}^T \mathcal{M} \left( \rho \mathbf{B} \ddot{\underline{\mathbf{U}}} + c \mathbf{B} \dot{\underline{\mathbf{U}}} + \mathbf{A} \underline{\mathbf{U}} \right) \mathcal{M} = \underline{\mathbf{v}}^T \mathcal{M} (\mathbf{B} \underline{\mathbf{f}} + \mathbf{B}_N \underline{\mathbf{t}} - \mathcal{L} \underline{\mathbf{u}}_D), \quad (18)$$

where an additional mask matrix  $\mathcal{M}$  is introduced to account for Dirichlet boundary conditions;  $\mathcal{M}$  is the diagonal matrix having zeros at nodes corresponding to  $\partial\Omega_D$  and ones everywhere else. Correspondingly,  $R_0^\mathcal{N}$  is the subspace of the vector space  $R^\mathcal{N}$  enforcing homogeneous Dirichlet boundary conditions. The term  $\mathbf{B}_N \underline{\mathbf{t}}$  in the right-hand side accounts for the surface integral  $\int_{\partial\Omega_N} \underline{\mathbf{t}} \cdot \underline{\mathbf{v}} d\Gamma$  arising from the traction boundary conditions, where  $\mathbf{B}_N$  is obtained from the mass matrix  $\mathbf{B}$  by zeroing out all the entries except for the ones corresponding to the nodes of  $\partial\Omega_N$ . The term  $\mathcal{L} \underline{\mathbf{u}}_D$  accounts for inhomogeneous Dirichlet boundary conditions, where  $\underline{\mathbf{u}}_D(t)$  is the expansion-coefficient vector of any function satisfying inhomogeneous Dirichlet boundary conditions  $\underline{\mathbf{v}}(\mathbf{x}, t)|_{\partial\Omega_D} = \underline{\mathbf{u}}_D(\mathbf{x}, t)$  and  $\mathcal{L} \underline{\mathbf{u}}_D = \rho \mathbf{B} \ddot{\underline{\mathbf{u}}}_D + c \mathbf{B} \dot{\underline{\mathbf{u}}}_D + \mathbf{K} \underline{\mathbf{u}}_D$ . This discrete variational problem is equivalent to solving the following system of equations for the vector  $\underline{\mathbf{U}}(t) \in R_0^\mathcal{N}$ :

$$\mathbf{M} \ddot{\underline{\mathbf{U}}} + \mathbf{C} \dot{\underline{\mathbf{U}}} + \mathbf{K} \underline{\mathbf{U}} = \underline{\mathbf{F}}, \quad (19)$$

where  $\mathbf{M} = \rho \mathcal{M} \mathbf{B} \mathcal{M}$ ,  $\mathbf{C} = c \mathcal{M} \mathbf{B} \mathcal{M}$ ,  $\mathbf{K} = \mathcal{M} \mathbf{A} \mathcal{M}$ , and  $\underline{\mathbf{F}} = \mathcal{M} (\mathbf{B} \underline{\mathbf{f}} + \mathbf{B}_N \underline{\mathbf{t}} - \mathcal{L} \underline{\mathbf{u}}_D)$ . The composite solution satisfying inhomogeneous

geneous Dirichlet boundary conditions is obtained as

$$\underline{\mathbf{u}}(t) = \underline{\mathbf{U}}(t) + \underline{\mathbf{u}}_D(t). \quad (20)$$

### 2.3. Temporal discretization

For temporal discretization, we employ a predictor/multicorrector Newmark algorithm [40]. This algorithm enforces the following relations between the displacements  $\underline{\mathbf{U}}_n$ , velocities  $\dot{\underline{\mathbf{U}}}_n$ , and accelerations  $\ddot{\underline{\mathbf{U}}}_n$  at the two consecutive times  $t_n = n \Delta t$  and  $t_{n-1} = (n-1) \Delta t$ , where  $\Delta t$  is the time step:

$$\begin{aligned} \dot{\underline{\mathbf{U}}}_n &= \dot{\underline{\mathbf{U}}}_{n-1} + \Delta t \left[ (1-\gamma) \ddot{\underline{\mathbf{U}}}_{n-1} + \gamma \ddot{\underline{\mathbf{U}}}_n \right], \\ \underline{\mathbf{U}}_n &= \underline{\mathbf{U}}_{n-1} + \Delta t \dot{\underline{\mathbf{U}}}_{n-1} + \frac{(\Delta t)^2}{2} \left[ (1-2\beta) \ddot{\underline{\mathbf{U}}}_{n-1} + 2\beta \ddot{\underline{\mathbf{U}}}_n \right]. \end{aligned} \quad (21)$$

The choice of  $\beta$  and  $\gamma$  determines particular properties of the method. For  $1/2 \leq \gamma \leq 2\beta$  the scheme achieves unconditional stability. Newmark originally proposed the constant-average-acceleration method (corresponding to the trapezoidal rule) with  $\beta = 1/4$ ,  $\gamma = 1/2$ , which corresponds to an unconditionally stable, second-order accurate scheme. These parameters are used in the current paper.

Equations (21) can be rewritten in terms of the increments. Thus, if we substitute into Eqs. (21)  $\ddot{\underline{\mathbf{U}}}_n = \ddot{\underline{\mathbf{U}}}_{n-1} + \Delta \ddot{\underline{\mathbf{U}}}_n$ , where  $\Delta \ddot{\underline{\mathbf{U}}}_n$  is the increment in acceleration, we get

$$\begin{aligned} \dot{\underline{\mathbf{U}}}_n &= \dot{\underline{\mathbf{U}}}_{n-1} + \Delta t \ddot{\underline{\mathbf{U}}}_{n-1} + \gamma \Delta t \Delta \ddot{\underline{\mathbf{U}}}_n, \\ \underline{\mathbf{U}}_n &= \underline{\mathbf{U}}_{n-1} + \Delta t \dot{\underline{\mathbf{U}}}_{n-1} + \frac{(\Delta t)^2}{2} \ddot{\underline{\mathbf{U}}}_{n-1} + \beta \Delta t^2 \Delta \ddot{\underline{\mathbf{U}}}_n. \end{aligned} \quad (22)$$

Equations of the form (22) suggest a convenient iterative approach to the implicit scheme (21). The algorithm is defined by distributing the increment

$\Delta \ddot{\underline{\mathbf{U}}}^n$  over  $k$  iterations  $\Delta \ddot{\underline{\mathbf{U}}}^n = \sum_{i=0}^k \Delta \ddot{\underline{\mathbf{U}}}^i_n$  and writing

$$\begin{aligned}\dot{\underline{\mathbf{U}}}^0_n &= \dot{\underline{\mathbf{U}}}_{n-1} + \Delta t \ddot{\underline{\mathbf{U}}}_{n-1} + \gamma \Delta t \Delta \ddot{\underline{\mathbf{U}}}^0_n, \\ \underline{\mathbf{U}}^0_n &= \underline{\mathbf{U}}_{n-1} + \Delta t \dot{\underline{\mathbf{U}}}_{n-1} + \frac{(\Delta t)^2}{2} \ddot{\underline{\mathbf{U}}}_{n-1} + \beta \Delta t^2 \Delta \ddot{\underline{\mathbf{U}}}^0_n\end{aligned}\quad (23)$$

for the predictor step, and

$$\begin{aligned}\ddot{\underline{\mathbf{U}}}^i_n &= \ddot{\underline{\mathbf{U}}}^{i-1}_n + \Delta \ddot{\underline{\mathbf{U}}}^i_n, \\ \dot{\underline{\mathbf{U}}}^i_n &= \dot{\underline{\mathbf{U}}}^{i-1}_n + \gamma \Delta t \Delta \ddot{\underline{\mathbf{U}}}^i_n, \\ \underline{\mathbf{U}}^i_n &= \underline{\mathbf{U}}^{i-1}_n + \beta (\Delta t)^2 \Delta \ddot{\underline{\mathbf{U}}}^i_n\end{aligned}\quad (24)$$

for  $i = 1, \dots, k$  corrector steps.

At the corrector steps, the increment in acceleration  $\Delta \ddot{\underline{\mathbf{U}}}^i_n$  is obtained from the substitution of Eqs. (24) into Eq. (19) to yield

$$\mathbf{M}^* \Delta \ddot{\underline{\mathbf{U}}}^i_n = \Delta \underline{\mathbf{F}}^i_n, \quad (25)$$

where

$$\mathbf{M}^* = \mathbf{M} + \gamma \Delta t \mathbf{C} + \beta (\Delta t)^2 \mathbf{K}. \quad (26)$$

The residual is obtained as

$$\Delta \underline{\mathbf{F}}^i_n = \underline{\mathbf{F}}_n - \mathbf{M} \ddot{\underline{\mathbf{U}}}^{i-1}_n - \mathbf{C} \dot{\underline{\mathbf{U}}}^{i-1}_n - \mathbf{K} \underline{\mathbf{U}}^{i-1}_n. \quad (27)$$

Since at the predictor step the value of acceleration increment  $\Delta \ddot{\underline{\mathbf{U}}}^0_n$  is unknown, it has to be specified a priori. Thus, different choices for the predictor step are possible, such as constant acceleration, constant velocity, or constant displacements [41]. In the current method, we use the constant

velocity predictor of the form  $\dot{\underline{\mathbf{U}}}_n^0 = \dot{\underline{\mathbf{U}}}_{n-1}$ , which essentially sets  $\Delta \ddot{\underline{\mathbf{U}}}_n^0 = -\ddot{\underline{\mathbf{U}}}_{n-1}/\gamma$  and leads to the following formulas:

$$\begin{aligned}\ddot{\underline{\mathbf{U}}}_n^0 &= -\frac{(1-\gamma)}{\gamma} \ddot{\underline{\mathbf{U}}}_{n-1}, \\ \dot{\underline{\mathbf{U}}}_n^0 &= \dot{\underline{\mathbf{U}}}_{n-1}, \\ \underline{\mathbf{U}}_n^0 &= \underline{\mathbf{U}}_{n-1} + \Delta t \dot{\underline{\mathbf{U}}}_{n-1} + \frac{(\Delta t)^2}{2} \left(1 - \frac{2\beta}{\gamma}\right) \ddot{\underline{\mathbf{U}}}_{n-1}.\end{aligned}\tag{28}$$

The iteration process is continued until either the maximum number of iterations  $k_{max}$  is reached or the convergence criterion  $\|\Delta \underline{\mathbf{F}}_n^i\| \leq \epsilon \|\Delta \underline{\mathbf{F}}_n^1\|$  is satisfied. The matrix equation (25) is solved at each iteration by using a conjugate gradient method. For steady problems, the equation

$$\mathbf{K}\underline{\mathbf{U}} = \underline{\mathbf{F}}\tag{29}$$

is solved once by using the conjugate gradient method.

### 3. Convergence Results: Steady Problems

Several test cases documenting a spatial convergence of the developed spectral-element algorithm for steady problems are presented in this section.

#### 3.1. Straight elements: bending of a beam (plane stress)

In the first test problem, we consider a bending of a narrow cantilever beam of rectangular cross-section under the end load. For this configuration, *plane stress* conditions can be assumed, reducing the problem to the two-dimensional case with Lamé coefficients given by Eqs. (7) and (9). An exact solution to this problem exists [42] and is given in Appendix Appendix A.1. We use length  $L = 10$ , width  $d = 1$ , Young's modulus  $E = 10000$ , and

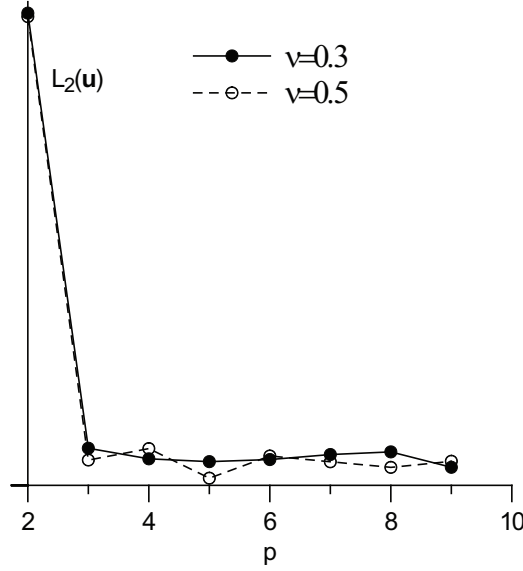


Figure 1: Bent beam and deflection of the centerline compared with the exact solution (symbols).

end load  $P = -3 I E / L^3$  ( $I$  is the cross-sectional moment of inertia) giving the end beam deflection  $v = -1$ . The boundary conditions are stress-free at the upper and lower edges, with parabolic shear stress distribution  $\tau_{xy} = -P(d^2/4 - y^2)/(2I)$  at the left edge ( $x = 0$ ) and displacements (or Dirichlet) boundary conditions at the right edge ( $x = L$ ). The computational domain consists of  $\mathcal{E} = 5$  rectangular elements. The bent beam and the deflection of the beam centerline compared with the exact solution are shown in Fig. 1 for  $\nu = 0.3$ ,  $p = 4$ . The agreement is excellent. To quantify the error with  $p$ -refinement, we plot the  $L_2(\mathbf{u})$  error versus the polynomial order in Fig. 2 for the values of  $\nu = 0.3$  and  $\nu = 0.5$ .

Since the analytical solution is the polynomial of degree 3, the SEM recovers it with machine accuracy for  $p = 3$  and higher; therefore it is meaningless to talk about the asymptotic rate of convergence with  $p$  [18]. Note that for plane stress elasticity, the incompressibility condition  $\nu = 0.5$  does not make the governing equations singular because it is  $1 - \nu$ , and not  $1 - 2\nu$  that appears in the denominator of  $\lambda$  (cf. Eqs. (8) and (9)). That explains why

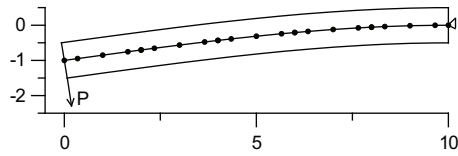


Figure 2:  $L_2(\mathbf{u})$  error versus the polynomial order for a narrow beam in plane stress.

the solution is recovered exactly for  $\nu = 0.5$  as well as for  $\nu = 0.3$  (Fig. 2) and there are no floating-point exceptions at  $\nu = 0.5$  in this case. Thus, plane stress loading does not represent a challenging test for Poisson locking and will not be considered further.

### 3.2. Straight elements: unit square (plane strain)

To consider a more challenging test for Poisson locking, we look at a two-dimensional *plane strain* problem, with  $\mu$  and  $\lambda$  defined by Eqs. (7) and (8). We consider a deformation of a unit square  $[0, 1] \times [0, 1]$ , with an exact solution for displacements listed in Appendix A.2. We choose the values  $A = (1 - \nu)/a$ ,  $B = -\nu/b$ . This choice corresponds to the most general but realistic loading with nonzero divergence

$$\operatorname{div} \mathbf{u} = (1 - 2\nu) \cos(ax) \cos(by),$$

which correctly reduces to zero in the incompressible case  $\nu = 0.5$ ; and with nonzero shear

$$\gamma_{xy} = -[(1 - \nu) b / a - \nu a / b] \sin(ax) \sin(by).$$

We set  $a = \pi/2$ ,  $b = \pi/3$ ,  $E = 1000$ , and we decompose the domain into four square elements of size  $h \times h$  with  $h = 0.5$ .

Following previous studies of locking properties of  $p$  and  $hp$ -FEM methods with nearly incompressible materials [16, 17, 18, 25, 32, 43], we document convergence of our SEM method in terms of the energy norm. Energy norm is defined as

$$\|\mathbf{u}\|_{energy, \nu} = (B_\nu(\mathbf{u}, \mathbf{u}))^{1/2}, \quad (30)$$

where  $B_\nu(\mathbf{u}, \mathbf{u})$  is the bilinear form of linear elasticity previously defined by Eq. (11). In Fig. 3 we plot the percentage relative error in the energy norm

$$(e_r)_{energy, \nu} = 100 \times \frac{\|\mathbf{u}_{numer} - \mathbf{u}_{exact}\|_{energy, \nu}}{\|\mathbf{u}_{exact}\|_{energy, \nu}} \quad (31)$$

versus the square root of a number of degrees of freedom  $N$  for different values of Poisson's ratio. The reason for plotting versus  $N^{1/2}$  is that when the exact solution is analytic on the solution domain, the rate of convergence of  $p$ -extensions is exponential [25]:

$$(e_r)_{energy, \nu} \leq \frac{k_e}{\exp(\gamma_e N^{1/d})}, \quad (32)$$

where  $k_e$  and  $\gamma_e$  are positive constants,  $k_e$  being dependent on Poisson's ratio, but  $\gamma_e$  not ( $d = 2, 3$  is the domain dimension). Results of Fig. 3 correspond well to the theoretical prediction of Eq. (32) and to the results obtained with

the  $p$ -version FEM (see, for example, [25], Fig. 3) including the existence of  $p_{crit}$  and the bounding envelope shown schematically in Fig. 3. The shape of the envelope depends on various factors, such as whether the elements are curved or triangular ( $p_{crit}$  is smaller for triangles than for quadrilaterals). No locking is observed for spectral element methods with straight elements, since the convergence rate does not depend on Poisson's ratio (error curves are parallel). However, convergence starts for higher values of the polynomial order as Poisson's ratio approaches 0.5, consistent with previous observations for the  $p$ -version FEM.

To investigate the influence of boundary conditions, we show the results for both traction (inhomogeneous Neumann) and displacement (inhomogeneous Dirichlet) boundary conditions, found as the corresponding values of the exact solution (Appendix A.4) at the boundaries. The same rate of convergence is observed with both traction and displacement boundary conditions, consistent with the existing mathematical proofs and numerical experiments for the  $p$ -version FEM [25, 31, 43].

### 3.3. Straight elements: unit cube

To document the spatial convergence in the full 3D case, we consider the deformation of a unit cube  $[0, 1] \times [0, 1] \times [0, 1]$ , with an exact solution given in Appendix A.3. With  $A = (1 - \nu)/a$ ,  $B = -0.5 \nu/b$ ,  $C = -0.5 \nu/c$ , we again recover a general loading situation with nonzero divergence,

$$\operatorname{div} \mathbf{u} = (1 - 2\nu) \cos(ax) \cos(by) \cos(cz),$$

approaching zero at  $\nu \rightarrow 0.5$ , and nonzero shear strain components  $\gamma_{xy}$ ,  $\gamma_{xz}$ ,  $\gamma_{yz}$ . We set  $a = \pi/2$ ,  $b = \pi/3$ ,  $c = \pi/4$ ,  $E = 1000$  and decompose the domain



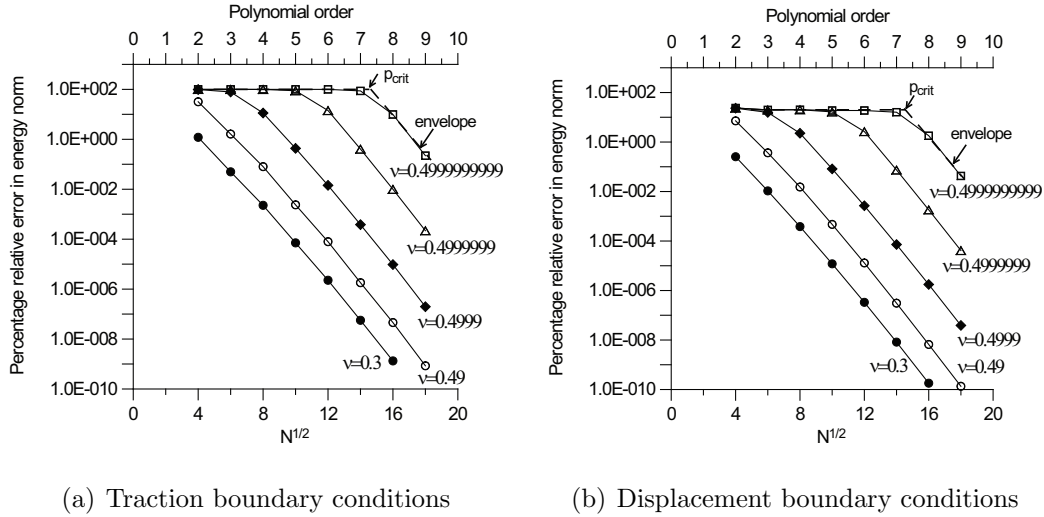


Figure 3: Convergence in the energy norm for a unit square.

into eight cubic elements of size  $h \times h \times h$  with  $h = 0.5$ . Note that most of the previous studies on locking with *hp*-FEM were confined to two dimensions and did not consider three-dimensional cases [16, 18, 25, 43]. Convergence in the energy norm versus the cubic root of a number of degrees of freedom  $N$  is plotted in Fig. 4 for both traction and displacement boundary conditions. The results are almost identical to those of a unit square, showing that the spatial dimension by itself does not influence the convergence and locking properties of the spectral element method, at least for straight elements.

### 3.4. Curved elements: hollow cylinder under internal pressure (plane strain)

To investigate the influence of curved elements on the method's spatial convergence, we look at the problems in cylindrical and spherical configurations. We first consider a long, thick-walled, hollow cylinder under internal pressure resulting in *plane strain* loading, with an exact solution given, for example, in [44] and documented in Appendix Appendix A.4. We set  $E = 1000$ ,

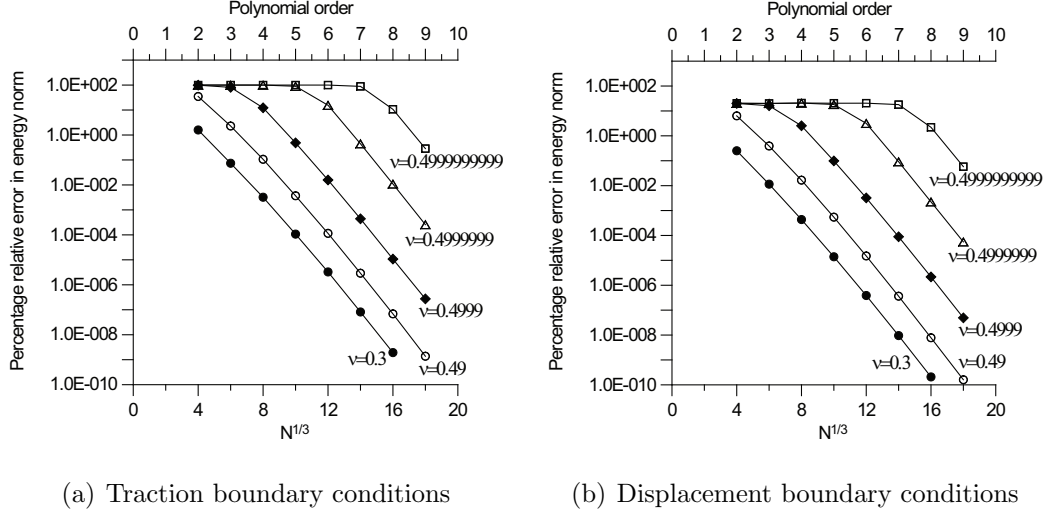
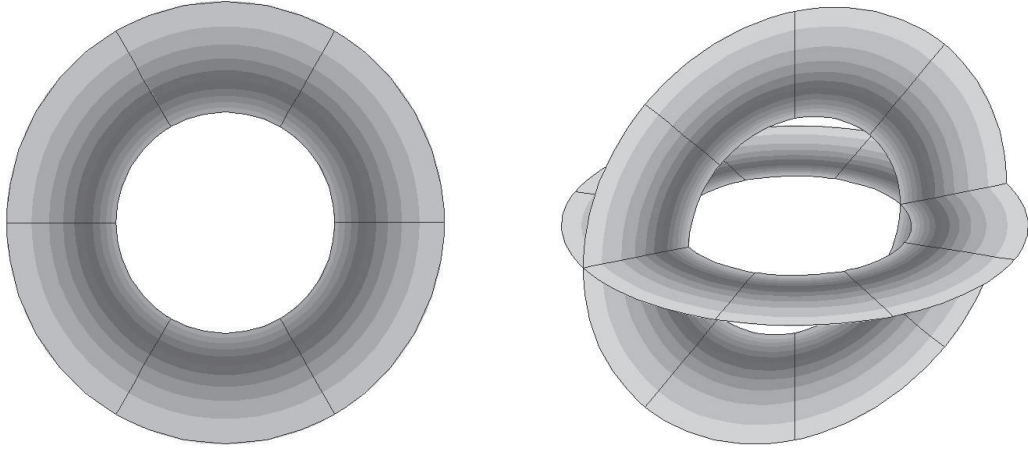


Figure 4: Convergence in the energy norm for a unit cube.

internal pressure  $P = 100$ , the inner and outer radii of the cylinder  $r_i = 0.5$  and  $r_o = 1$ . Because of the plane strain loading, this problem can be considered in 2D. The computational domain consists of a hollow disk with six circumferential elements of the radial width  $h = 0.5$ . The computational domain and solution (radial displacement for  $\nu = 0.3$ ) are shown in Fig. 5a. Convergence in the energy norm versus  $N^{1/2}$  is shown in Fig. 6 for traction and displacement boundary conditions. Although more severe locking effects for curved elements compared with straight elements were observed in [16, 18] with  $hp$  finite-element methods, the current study does not show significant deterioration in convergence rates as a result of locking. Note that special care has been taken here to ensure that the location of the grid nodes and the GLL points is exact with the double precision in cylindrical coordinates. The major effect of the curved elements is to increase the polynomial degree at which the error drops down to machine accuracy for compressible mate-



(a) Hollow cylinder. Min displacement 0.05 (at  $r_0$ ); max displacement 0.1 (at  $r_i$ ).

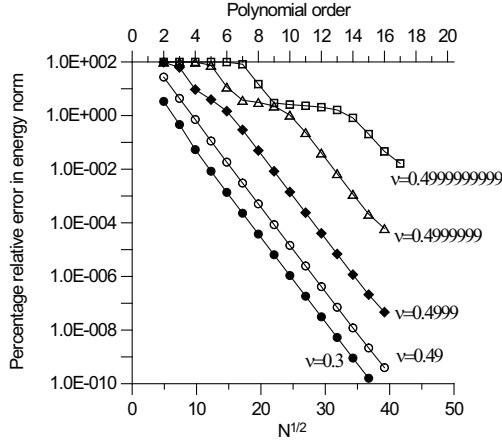
(b) Hollow sphere. Min displacement 0.01 (at  $r_0$ ); max displacement 0.04 (at  $r_i$ ).

Figure 5: Meshes with curved elements. Radial displacement  $u_r$  is shown.

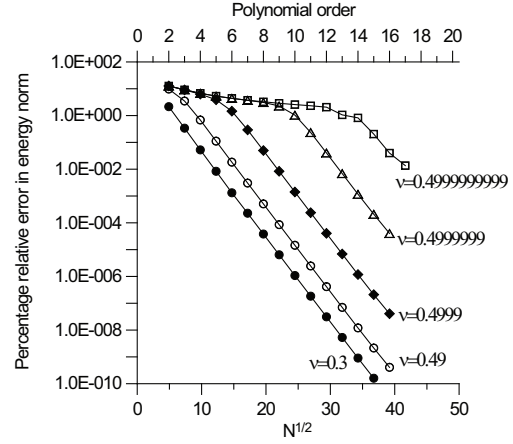
rials and, as a consequence, to increase  $p_{crit}$  and to change the shape of the bounding envelope for incompressible materials, as discussed in Sec. 3.2.

### 3.5. Curved elements: hollow sphere under internal pressure

Our last example with steady elasticity problems is a 3D loading case with curved elements, namely, that of a thick-walled hollow sphere under internal pressure, with an exact solution given in Appendix Appendix A.5. Note that a spherical domain is a more stringent case than those considered in previous 2D studies of locking with  $hp$ -FEM [16, 18, 25, 43]. We set  $E = 1000$ ,  $P = 100$ , spherical shell radii  $r_i = 0.5$ , and  $r_o = 1$ ; the domain consists of 24 elements with the radial width  $h = 0.5$ . Two orthogonal cross-sections of the sphere and the radial displacement for  $\nu = 0.3$  are shown in Fig. 5b. Convergence in the energy norm versus  $N^{1/3}$  is shown in Fig. 7 for

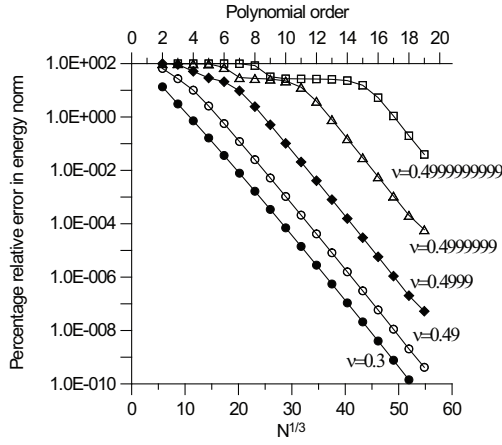


(a) Traction boundary conditions

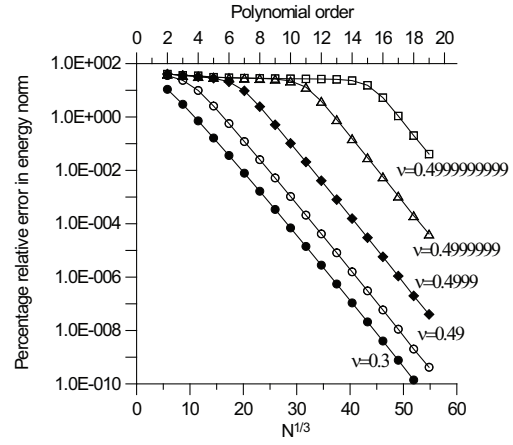


(b) Displacement boundary conditions

Figure 6: Convergence in the energy norm for the hollow cylinder.



(a) Traction boundary conditions



(b) Displacement boundary conditions

Figure 7: Convergence in the energy norm for the hollow sphere.

traction and displacement boundary conditions. Conclusions similar to that of the cylindrical shell domain stay valid, confirming the absence of the effect of problem dimension on the locking properties of the method, as observed with the straight elements.

#### 4. Convergence Results: Unsteady Problem

As an example of an unsteady problem, we choose a previously studied configuration of a unit square in plane-strain conditions, but with non-zero density. In this case, because of inertia effects, the displacements are the oscillatory functions; and if damping is present, they also decay in time, with the frequency and the rate of decay given in Appendix Appendix A.6. We set Young's modulus  $E = 1000$  and the domain  $[0, 1] \times [0, 1]$  decomposed into four square elements, as in the corresponding steady example, and choose  $a = \pi/3$ ,  $\rho = 1000$ ,  $A = 1$ , and two values of damping coefficient:  $c = 0$ , corresponding to no damping, and  $c = 100$ , corresponding to the addition of damping. Note that a more general time-dependent solution could be constructed, with  $b \neq a$  and  $B \neq -A$  (see the corresponding solution for a steady unit square), but this would lead either to two displacement functions,  $u$  and  $v$ , oscillating with different frequencies (thus making divergence-free constraint impossible to satisfy at every moment in time), or to frequency being a function of  $\lambda$  and  $\mu$ , rather than just  $\mu$ , becoming infinite at  $\nu \rightarrow 0.5$ . Although such solutions could exist for  $\nu \neq 0.5$ , they would not be valid in the nearly incompressible case of  $\nu \rightarrow 0.5$  and are therefore not considered here.

Exact and numerical solutions for a long-time integration ( $t = 100$ ) for

the axial displacement for both undamped and damped cases are presented in Fig. 8 ( $\nu = 0.3$ ,  $p = 5$ , and  $\Delta t = 0.1$  are used). The exact and numerical solutions are virtually indistinguishable. Spatial convergence versus  $N^{1/2}$  at  $t = 10$  is presented in Fig. 9 for both undamped and damped cases for a range of Poisson's ratios. We present results for traction boundary conditions; results for displacement boundary conditions are essentially the same (cf. Figs. 3 and 4). As in the steady problem with straight elements, no locking is observed in the time-dependent problem for both the undamped and damped cases, with the same convergence rate as in the steady problem. The only difference is that the minimum error that can be achieved by  $p$ -refinement is now controlled by the time step (spatial convergence stops when the polynomial degree is high enough that the spatial error drops below the temporal error). One can see that the minimum error (controlled by the temporal error) drops by two orders of magnitude when the time step is reduced by one order of magnitude, consistent with the second-order accuracy of the Newmark temporal discretization scheme. The temporal convergence at polynomial degree  $p = 8$  is shown in Fig. 10. For lower Poisson's ratios, the expected second-order temporal convergence is observed for all the time steps. As Poisson's ratio increases, second-order convergence is still observed for larger time steps, but it deteriorates for smaller time steps. This deterioration can be explained by the fact that for large time steps, the temporal error dominates, and we observe the expected second-order temporal convergence, whereas for small time steps, the spatial error becomes dominant, a situation that does not change with further reduction in time-step size and thus slows or stops the temporal convergence. Since spatial errors are gener-

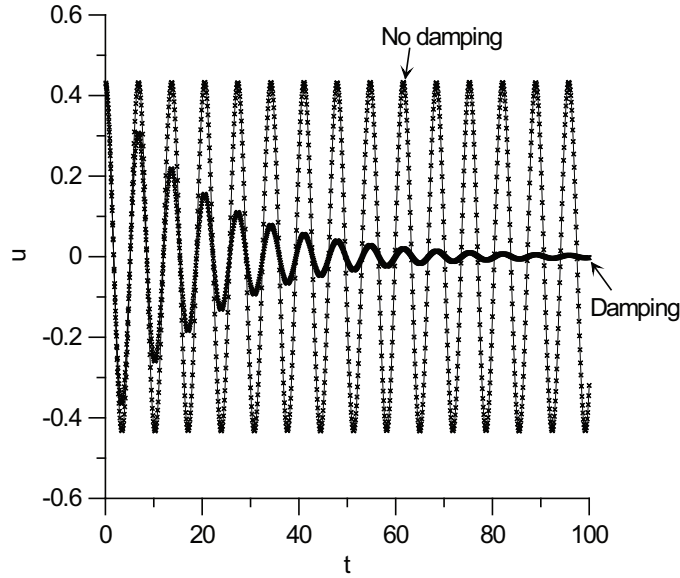


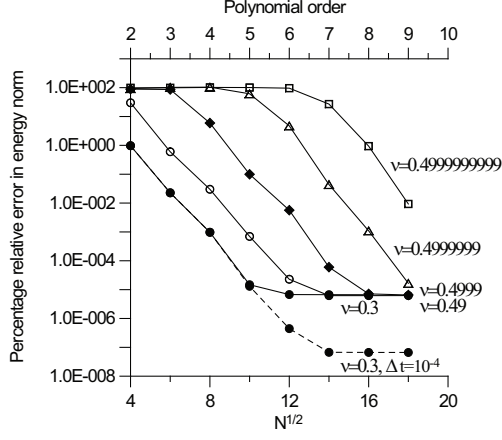
Figure 8: Axial displacement versus time for undamped and damped cases. Lines correspond to exact solution, symbols to numerical solution.

ally higher for higher Poisson’s ratios for the same  $p$  (see Figs. 3 and 9), this “temporal locking” behavior is observed only for high Poisson’s ratios.

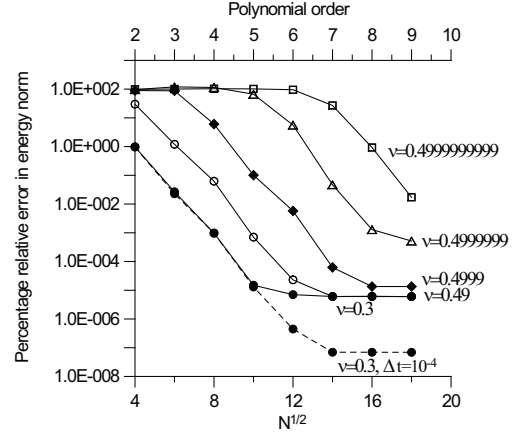
Note that this study is, to our knowledge, the first in the open literature that addresses the issue of Poisson locking for time-dependent problems with finite or spectral element methods.

## 5. Conclusions

In this paper, we investigate convergence properties of the Legendre spectral element approximation of displacement formulation of the linear elasticity equations for a range of Poisson’s ratios from a compressible regime ( $\nu = 0.3$ ) to nearly incompressible regime ( $\nu = 0.4999999999$ ). Several numerical experiments are considered, including problems with straight elements in 2D (plane stress and plane strain) and 3D regimes, problems with curved elements in 2D and 3D, and an unsteady problem. For steady problems with both straight and curved elements, we demonstrate exponential convergence with  $p$ -refinement independent of Poisson’s ratio, showing that

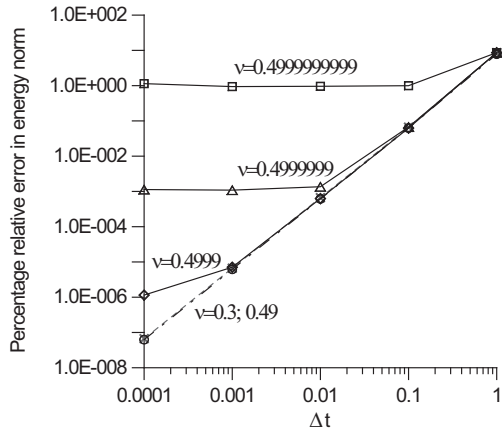


(a) Undamped case

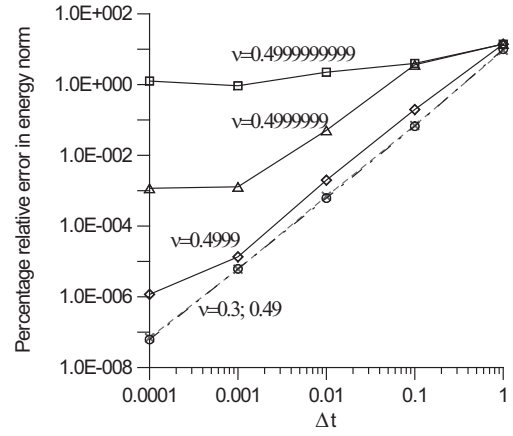


(b) Damped case

Figure 9: Spatial convergence in the energy norm for a time-dependent problem in a unit square,  $\Delta t = 10^{-3}$ .



(a) Undamped case



(b) Damped case

Figure 10: Temporal convergence in the energy norm for a time-dependent problem in a unit square,  $p = 8$ .



high-order methods are free from the locking phenomenon inherent in low-order methods, consistent with previous observations with finite elements. The effect of the curved elements is to increase the polynomial degree at which the error drops down to machine accuracy for compressible materials and, as a consequence, to increase  $p_{crit}$  and to push the bounding envelope associated with locking to the right for incompressible materials. We also show for the first time that locking properties with respect to  $p$ -refinement are unchanged when the time-dependent problems are considered, but “temporal locking” can be observed for high Poisson’s ratios with respect to temporal refinement due to the dominance of spatial errors.

## Acknowledgments

We acknowledge the financial support of this work by NSF RTG grant DMS-0636574 and the SHARP project of the U.S. Department of Energy, under Contract DE-AC02-06CH11357.

## Appendix A. Exact Solutions to the Test Problems

### *Appendix A.1. Bending of a narrow cantilever beam*

For the bending of a narrow cantilever beam with rectangular cross-section of length  $L$  and height  $d$ , under the end load  $P$  applied at  $x = 0$  and fixed at the point  $x = L, y = 0$ , the following exact solution exists for

the horizontal displacement  $u$  and the vertical displacement  $v$  [42]:

$$u = -\frac{P}{2EI}x^2y + \frac{P}{3EI}\left(1 + \frac{\nu}{2}\right)y^3 + \frac{P}{2EI}\left[L^2 - (1 + \nu)\frac{d^2}{2}\right]y, \quad (\text{Appendix A.1})$$

$$v = \frac{\nu P}{2EI}xy^2 + \frac{P}{6EI}x^3 - \frac{PL^2}{2EI}x + \frac{PL^3}{3EI}. \quad (\text{Appendix A.2})$$

Here  $I = d^3/12$  is the cross-sectional moment of inertia.

#### *Appendix A.2. Deformation of a unit square*

For a unit square  $[0, 1] \times [0, 1]$  in plane strain conditions under forcing

$$\begin{aligned} f_x &= [(Aa^2 + Babb)(\lambda + \mu) + A(a^2 + b^2)\mu] \sin(ax) \cos(by), \\ f_y &= [(Bb^2 + Aabb)(\lambda + \mu) + B(a^2 + b^2)\mu] \cos(ax) \sin(by), \end{aligned} \quad (\text{Appendix A.3})$$

the following exact solutions exist:

$$\begin{aligned} u &= A \sin(ax) \cos(by), \\ v &= B \cos(ax) \sin(by). \end{aligned} \quad (\text{Appendix A.4})$$

#### *Appendix A.3. Deformation of a unit cube*

For a unit cube  $[0, 1] \times [0, 1] \times [0, 1]$  under forcing

$$\begin{aligned} f_x &= A_x \sin(ax) \cos(by) \cos(cz), \\ f_y &= A_y \cos(ax) \sin(by) \cos(cz), \\ f_z &= A_z \cos(ax) \cos(by) \sin(cz), \end{aligned} \quad (\text{Appendix A.5})$$

where

$$\begin{aligned}
A_x &= (A a^2 + B a b + C a c)(\lambda + \mu) + A(a^2 + b^2 + c^2)\mu, \\
A_y &= (B b^2 + A a b + C b c)(\lambda + \mu) + B(a^2 + b^2 + c^2)\mu, \\
A_z &= (C c^2 + A a c + B b c)(\lambda + \mu) + C(a^2 + b^2 + c^2)\mu,
\end{aligned}
\tag{Appendix A.6}$$

the solutions are

$$\begin{aligned}
u &= A \sin(ax) \cos(by) \cos(cz), \\
v &= B \cos(ax) \sin(by) \cos(cz), \\
w &= C \cos(ax) \cos(by) \sin(cz).
\end{aligned}
\tag{Appendix A.7}$$

#### *Appendix A.4. Hollow cylinder under internal pressure*

For a plane strain hollow cylinder with the inner radius  $r_i$  and the outer radius  $r_o$  under internal pressure  $P$  and zero external pressure (satisfying boundary conditions  $\sigma_r(r_i) = -P$ ,  $\sigma_r(r_o) = 0$ ), the displacements in cylindrical coordinates have the form [44]

$$\begin{aligned}
u_r &= \frac{1 + \nu}{E} \frac{P r_i^2}{r_o^2 - r_i^2} \left[ (1 - 2\nu) r + \frac{r_o^2}{r} \right], \\
u_\theta &= 0, \quad u_z = 0.
\end{aligned}
\tag{Appendix A.8}$$

#### *Appendix A.5. Hollow sphere under internal pressure*

For a hollow sphere with the inner radius  $r_i$  and the outer radius  $r_o$  under internal pressure  $P$  and zero external pressure (satisfying boundary conditions  $\sigma_r(r_i) = -P$ ,  $\sigma_r(r_o) = 0$ ), the displacements in spherical coordinates

have the form (see [45])

$$u_r = \frac{1}{E} \frac{P r_i^3}{r_o^3 - r_i^3} \left[ (1 - 2\nu) r + (1 + \nu) \frac{r_o^3}{2 r^2} \right],$$

$$u_\theta = 0, \quad u_\phi = 0. \quad (\text{Appendix A.9})$$

#### Appendix A.6. Vibrating unit square

For a unit square  $[0, 1] \times [0, 1]$  with the density  $\rho$  and the damping  $c$  in plane strain conditions with  $f_x = f_y = 0$  and appropriate initial and boundary conditions, the exact time-dependent solution can be found as

$$u = A \sin(ax) \cos(ay) \cos(\omega t) e^{-\beta t},$$

$$v = -A \cos(ax) \sin(ay) \cos(\omega t) e^{-\beta t}, \quad (\text{Appendix A.10})$$

where

$$\beta = \frac{c}{2\rho}, \quad \omega = \sqrt{\beta^2 + \frac{(\alpha - c\beta)}{\rho}}, \quad \alpha = 2a^2\mu. \quad (\text{Appendix A.11})$$

- [1] A. T. Patera. A spectral element method for fluid dynamics: Laminar flow in a channel expansion. *J. Comp. Phys.*, 54:468–488, 1984.
- [2] P. F. Fischer and A. T. Patera. Parallel spectral element solution of the Stokes problem. *J. Comp. Phys.*, 92:380–421, 1991.
- [3] M. O. Deville, P. F. Fischer, and E. H. Mund. *High-order methods for incompressible fluid flow*. Cambridge University Press, Cambridge, UK, 2002.
- [4] L. F. Pavarino and O. B. Widlund. Iterative substructuring methods for spectral element discretization of elliptic systems, I: Compressible linear elasticity. *SIAM J. Numer. Anal.*, 37:2:375–402, 2000.

- [5] L. F. Pavarino and O. B. Widlund. Iterative substructuring methods for spectral element discretization of elliptic systems, II: Mixed methods for linear elasticity and Stokes flow. *SIAM J. Numer. Anal.*, 37:2:353–374, 2000.
- [6] F. Casadei, E. Geabellini, G. Fotia, F. Maggio, and A. Quarteroni. A mortar spectral/finite element method for complex 2D and 3D elastodynamics problems. *Comp. Meth. Appl. Mech. Eng.*, 191:5119–5148, 2002.
- [7] M. Stupazzini and C. Zambelli. GeoELSEvp: A spectral element approach for dynamic elasto-viscoplastic problems. *Rivista Italiana di Geotecnica*, 4:71–81, 2005.
- [8] S. Dong and Z. Yosibash. A parallel spectral element method for dynamic three-dimensional nonlinear elasticity problems. *Comput. Struct.*, 87:59–72, 2009.
- [9] D. Komatitsch, S. Tsuboi, and J. Tromp. The spectral-element method for elastic wave equations – application to 2D and 3D seismic problems. *Int. J. Numer. Meth. Eng.*, 45:1139–1164, 1999.
- [10] E. Chaljub, Y. Capdeville, and J-P. Vilotte. Solving elastodynamics in a fluid-solid heterogeneous sphere: A parallel spectral element approximation on non-conforming grids. *J. Comp. Phys.*, 187:457–491, 2003.
- [11] D. Komatitsch, S. Tsuboi, and J. Tromp. The spectral-element method in seismology. *Geophysical Monograph*, 57:205–227, 2005.

- [12] J. C. Brigham, W. Aquino, M. A. Aguilo, and P. J. Diamessis. A spectral finite element approach to modeling soft solids excited with high-frequency harmonic loads. *Comp. Meth. Appl. Mech. Eng.*, 200:692–698, 2011.
- [13] S. Ha and F-K. Chang. Optimizing a spectral element for modeling PZT-induced Lamb wave propagation in thin plates. *Smart Mater. Struct.*, 19, 2010.
- [14] B. Szabó and I. Babuška. *Finite-element analysis*. John Wiley & Sons, New York, 1991.
- [15] T. J. R. Hughes. *The finite element method*. Dover: New York, 2000.
- [16] L. Chilton and M. Suri. On the selection of a locking-free *hp* element for elasticity problems. *Int. J. Numer. Meth. Eng.*, 40:2045–2062, 1997.
- [17] I. Babuška and M. Suri. Locking effects in the finite element approximation of elasticity problems. *Numer. Math.*, 62:439–463, 1992.
- [18] M. Suri. Analytical and computational assessment of locking in the *hp* finite element method. *Comp. Methods Appl. Mech. Eng.*, 133:347–371, 1996.
- [19] P. H. Mott, J. R. Dorgan, and C. M. Roland. The bulk modulus and Poisson’s ratio of “incompressible” materials. *J. Sound and Vibr.*, 312:572–575, 2008.
- [20] J. D. Humphrey. Review paper: Continuum biomechanics of soft biological tissues. *Proc. R. Soc. Lond. A*, 459:3–46, 2003.

- [21] E. B. Shim and R. D. Kamm. Numerical simulation of steady flow in a compliant tube or channel with tapered wall thickness. *J. Fluids Struct.*, 16:1009–1027, 2002.
- [22] P. H. Mott, J. R. Dorgan, and C. M. Roland. A coupled momentum method for modeling blood flow in three-dimensional deformable arteries. *Comput. Methods Appl. Mech. Eng.*, 195:5685–5706, 2006.
- [23] A. Valencia and F. Solis. Blood flow dynamics and arterial wall interaction in a saccular aneurysm model of the basilar artery. *Comput. Struct.*, 84:1326–1337, 2006.
- [24] S. Gopalakrishnan. Behavior of isoparametric quadrilateral family of Lagrangian fluid elements. *Int. J. Numer. Meth. Eng.*, 54:731–761, 2002.
- [25] B. A. Szabó, I. Babuška, and B. K. Chayapathy. Stress computations for nearly incompressible materials by the  $p$ -version of the finite element method. *Int. J. Numer. Meth. Eng.*, 28:2175–2190, 1989.
- [26] H. S. Yu, G. T. Houlsby, and H. J. Burd. A novel isoparametric finite element displacement formulation for axisymmetric analysis of nearly incompressible materials. *Int. J. Numer. Meth. Eng.*, 36:2454–2472, 1993.
- [27] J. C. Nagtegaal, D. M. Parks, and J. R. Rice. On numerically accurate finite element solutions in the fully plastic range. *Comp. Meth. Appl. Mech. Eng.*, 4:1530–177, 1974.
- [28] D. S. Malkus and T. J. R. Hughes. Mixed finite element methods –

- reduced and selective integration techniques: a unification of concepts. *Comp. Meth. Appl. Mech. Eng.*, 12:67–76, 1978.
- [29] G. Prathap. *The finite element method in structural mechanics*. Kluwer Academic Press: Dordrecht, 1993.
  - [30] F. Brezzi and M. Fortin. *Mixed and hybrid finite element methods*. Springer, Berlin, 1991.
  - [31] M. Vogelius. An analysis of the  $p$ -version of the finite element method for nearly incompressible materials: Uniformly valid, optimal error estimates. *Numer. Math.*, 41:39–53, 1983.
  - [32] U. Heisserer, S. Hartmann, A. Duster, and Z. Yosibash. On volumetric locking-free behavior of  $p$ -version finite elements under finite deformations. *Comm. Numer. Meth. Eng.*, 24:1019–1032, 2008.
  - [33] L. F. Pavarino. Preconditioned mixed spectral element methods for elasticity and Stokes problems. *SIAM J. Sci. Comp.*, 19:375–402, 1997.
  - [34] L. F. Pavarino, O. B. Widlund, and S. Zampini. BDDC preconditioners for spectral element discretizations of almost incompressible elasticity in three dimensions. *SIAM J. Numer. Anal.*, 32:6:3604–3626, 2010.
  - [35] M. A. Sprague and T. L. Geers. Legendre spectral finite elements for structural dynamics analysis. *Comm. Numer. Meth. Eng.*, 00:1–13, 2007.
  - [36] K. D. Brito and M. A. Sprague. Reissner-Mindlin Legendre spectral finite elements with mixed reduced quadrature. *Comp. Mech.*, in review, 2011.



- [37] G. E. Karniadakis and S. J. Sherwin. *Spectral/hp element methods for computational fluid dynamics*. 2nd ed. Oxford University Press, New York, 2005.
- [38] P. F. Fischer. An overlapping Schwarz method for spectral element solution of the incompressible Navier-Stokes equations. *J. Comp. Phys.*, 133:84–101, 1997.
- [39] S. A. Orszag. Spectral methods for problems in complex geometries. *J. Comput. Phys.*, 37:70–92, 1980.
- [40] N. M. Newmark. A method of computation for structural dynamics. *Journal of Engineering Mechanics, ASCE*, 85:67–94, 1959.
- [41] J. A. Cottrell, T. J. R Hughes, and Y. Bazilevs. *Isogeometric analysis: Toward integration of CAD and FEA*. Wiley, Chichester, U.K., 2009.
- [42] C.-T. Wang. *Applied elasticity*. McGraw-Hill, New York, 1953.
- [43] Z. Yosibash. Accurate stress extraction for nearly incompressible materials by the displacement formulation of the p-version FEMn. *Comm. Numer. Meth. Eng.*, 12:807–826, 1996.
- [44] X.-L. Gao. Elasto-plastic analysis of an internally pressurized thick-walled cylinder using a strain gradient plasticity theory. *Int. J. Solids Struct.*, 40:6445–6455, 2003.
- [45] Y. C. Fung. *Foundations of solid mechanics*. Prentice Hall, Englewood Cliffs, N.J., 1965.

The following should be removed before publication: The submitted manuscript has been created by UChicago Argonne, LLC, Operator of Argonne National Laboratory ("Argonne"). Argonne, a U.S. Department of Energy Office of Science laboratory, is operated under Contract No. DE-AC02-06CH11357. The U.S. Government retains for itself, and others acting on its behalf, a paid-up nonexclusive, irrevocable worldwide license in said article to reproduce, prepare derivative works, distribute copies to the public, and perform publicly and display publicly, by or on behalf of the Government.